

The Impact of Assembly State on the Defect Tolerance of TMV-based Light Harvesting Arrays

Rebekah A. Miller, Nicholas Stephanopoulos, Jesse M. McFarland, Andrew S. Rosko,
Phillip L. Geissler, and Matthew B. Francis*

*Department of Chemistry, University of California, Berkeley, CA 94720-1460, and Material
Science Division, Lawrence Berkeley National
Labs, Berkeley, CA 94720-1460*

Supporting Information and Figures

Experimental:

Construction of TMVP Expression Plasmids. pTMV0041, a wild-type TMV cDNA clone, was received as a gift from Dr. Dennis Lewandowski, University of Florida. Standard recombinant techniques were used to construct an expression plasmid with pET20b vector DNA (Novagen). The TMVP gene was amplified by PCR, using an upstream primer with the sequence 5'-GATTCGTTTTACATATGTCTTAC-3' and a downstream primer with the sequence 5'-TAGTACCATGGCATCTTGACTAC-3'. The amplification product was digested with NdeI and NcoI (NEB) before ligation into pET20b with T4 DNA ligase (NEB). A TMVP-S123C mutant construct was made using standard recombinant techniques.

Expression and Purification of Recombinant TMV Coat Protein (TMVP). TMVP was expressed and purified according to a modified literature procedure.¹ Tuner DE3pLysS competent cells (Novagen) were transformed with pTMVP, and colonies were selected for inoculation of Terrific Broth cultures. When cultures reached mid-log phase as determined by O.D. 600, expression was induced by addition of 10 μ M IPTG (Invitrogen). Cultures were grown 14-18 hr at 30 °C, harvested by centrifugation, and stored at -80 °C.

Induced cells were thawed and resuspended in ice-cold Buffer A (20 mM Tris, pH = 7.2; 5 mM DTT; 20 mM NaCl) containing 1 mM Pefabloc SC (Roche). Cells were lysed by sonication (Branson Ultrasonics), and the resulting lysate was cleared by ultracentrifugation for 50 min at 40,000 rpm in a Beckman 40 Ti rotor. The cleared lysate was applied to a DEAE anion-exchange column (Amersham) and eluted with Buffer A at 4 °C. Fractions were analyzed by SDS-PAGE, and fractions containing TMVP were combined, concentrated, and dialyzed against 50 mM sodium citrate buffer, pH = 3.5. The resulting TMVP precipitate was collected by centrifugation, washed with additional citrate buffer, and resuspended in Buffer B (100 mM Tris, pH 8). The purified TMVP was quantified by Bradford assay,² flash-frozen, and stored at -20 °C.

General Procedure for Chromophore Attachment. A thawed aliquot of TMVP (8.0 mg/mL in 100 mM HEPES buffer, pH 6.5, 1% TCEP) was exchanged into 100 mM KH₂PO₄, pH 7, using a NAP-10 column. The solution was diluted to 1.5 mg/mL in TMVP, and 5 equivalents of maleimide-functionalized chromophore were added as a DMF solution (up to 5%, v/v). In optimization experiments, the higher DMF concentrations, increased equivalents of the dye, or

extended reaction times led to over-labeling, presumably at the native C27 residue. The reaction mixture was vortexed briefly and left at room temperature for 15 – 20 minutes. The reaction was quenched with 20 equivalents of β -mercaptoethanol, and the mixture was passed through a NAP-10 column to remove excess chromophore. Conversion of TMVP to modified product was monitored by LC/ESI-MS and UV-visible spectroscopy. Reactions involving smaller molecular weight dyes, such as Oregon Green 488, required a shorter reaction time compared to those involving larger dyes, such as Alexa Fluor 594. The site selectivity of the modification reaction was confirmed through mass spectrometry analysis of peptide fragments after digestion with trypsin.

Assembly of TMVP disks and rods. Solutions of dye-modified TMVP monomers were diluted to 0.75 mg/mL and dialyzed overnight against 25 mM phosphate buffer, pH 8, to achieve equilibration to the monomer state. After dialysis, TMVP mixtures were analyzed by size exclusion chromatography using an HPLC equipped using a Phenomenex PolySep-GFC-P 5000 column (300 x 7.8 mm, flow rate 1.0 ml/min) equilibrated with 25 mM phosphate buffer, pH 8. The concentration of dye-modified TMVP monomers was quantified using a Bradford assay.² The monomers were combined in the stoichiometric ratios and allowed to equilibrate for 3 hours at room temperature to allow for exchange between any preformed small aggregates before assembly. For assembly into rods, monomer solutions were exchanged into 100 mM sodium acetate buffer, pH 5.5, and dialyzed overnight. After dialysis, the conversion to larger structures was monitored by size exclusion chromatography, and the assemblies were characterized visually using TEM.

Chemical bleaching of chromophores. In a 10 mL Falcon tube, 2 mL of protein solution (57 μ M in 100 mM phosphate, pH 7.0), was combined with 5 mg solid NaBH₄. Fluctuations in pH were mediated through the dropwise addition of 3 M NaOH or 8 M HCl to maintain a pH between 6 and 8. The solution was incubated at 4 °C for 12-18 h. A portion of the resulting mixture was diluted two-fold with ddH₂O and analyzed by high resolution mass spectrometry and size exclusion chromatography. For the Ir-mediated bleaching of chromophores, 2 mL of protein solution (57 μ M in 100 mM phosphate, pH 7.0), was combined with 200 μ L of a stock solution containing 1 M formate and 1 M phosphate at pH 6.5 in a 10 mL Falcon tube. Next 5 μ L of catalyst solution (5.0 mM in ddH₂O) were then added, and the solution was incubated at 25 °C for 1-5 h. A portion of the resulting mixture was diluted two-fold with ddH₂O and analyzed by high resolution mass spectrometry and size exclusion chromatography.

Synthesis of Cp*Ir(4,4'-dimethoxy-2,2'-bipyridine)Cl. An adapted procedure of Dadci, et al was used for synthesis of the Ir catalyst.³ Dichloro(pentamethylcyclopentadienyl)iridium (III) dimer (16.0 mg, 20.1 μ mol), 4,4'-dimethoxy-2,2'-bipyridine (8.7 mg, 40.2 μ mol) and 2 mL of methanol were combined in a scintillation vial charged with a magnetic stir bar. The heterogeneous mixture was stirred at room temperature until it became homogeneous (<10 min). The solution was concentrated under reduced pressure and the residue was re-dissolved in a minimum amount of methylene chloride. The product was then precipitated by the dropwise addition of hexanes until no more precipitate appeared. The precipitate was collected by filtration, washed with three 1 mL portions of hexanes and dried *in vacuo* to yield the product as a light yellow solid.

High resolution mass spectrometry. The LC was connected online to a quadrupole time-of-flight (Q-TOF) mass spectrometer equipped with a Z-spray electrospray ionization (ESI) source (Q-ToF Premier, Waters). The ion source parameters were as follows: ESI capillary voltage 2.4 kV, nebulizing gas (nitrogen) flow rate 800 L/hr, sample cone voltage 30 V, extraction cone voltage 3 V, ion guide voltage 1 V, source block temperature 80 °C, and nebulizing gas temperature 200 °C. No cone gas was used. The TOF analyzer was operated in “V” mode. Under these conditions, a mass resolving power of 1.0×10^4 was routinely achieved, which is sufficient to resolve the isotopic distributions of the modified and unmodified peptide ions under investigation. Thus, an ion’s mass and charge could be determined independently, i.e., the ion charge was determined from the reciprocal of the spacing between adjacent isotope peaks in the m/z spectrum. External mass calibration was performed immediately prior to measuring samples, using solutions of sodium formate. Survey scans were acquired over the range m/z 100–2000 using a 1.0 s scan integration and a 0.05 s inter-scan delay.

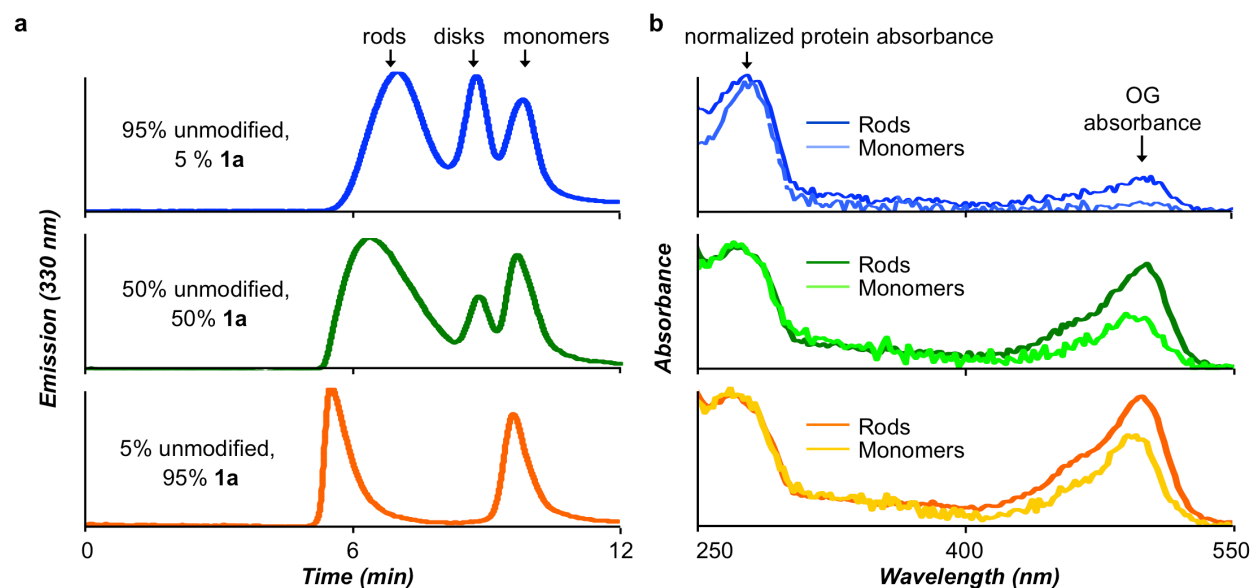


Figure S1. Effect of chromophore modification on assembly. (a) Size exclusion chromatograms for three systems differing in the extent of modification. (b) A comparison of the absorbance spectrum of the rod and monomer peaks for each of the three systems, normalized at the protein absorbance (280 nm).

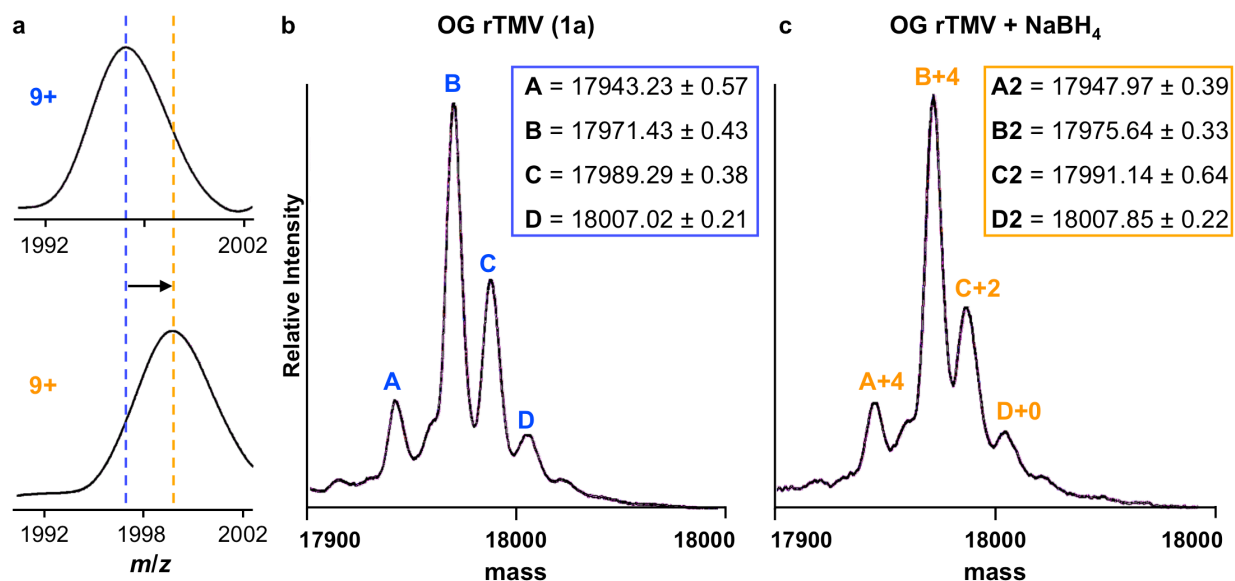


Figure S2. High resolution mass spectrometry data for S123C TMVP modified with **1** and the same construct after undergoing bleaching by NaBH₄. (a) A mass shift was observed throughout the charge ladder upon bleaching. Data for the 9+ charge state are shown for the construct before (top) and after (bottom) bleaching. (b) The reconstructed mass for TMVP modified with OG. (c) The reconstructed mass for TMVP modified with OG after exposure to NaBH₄.

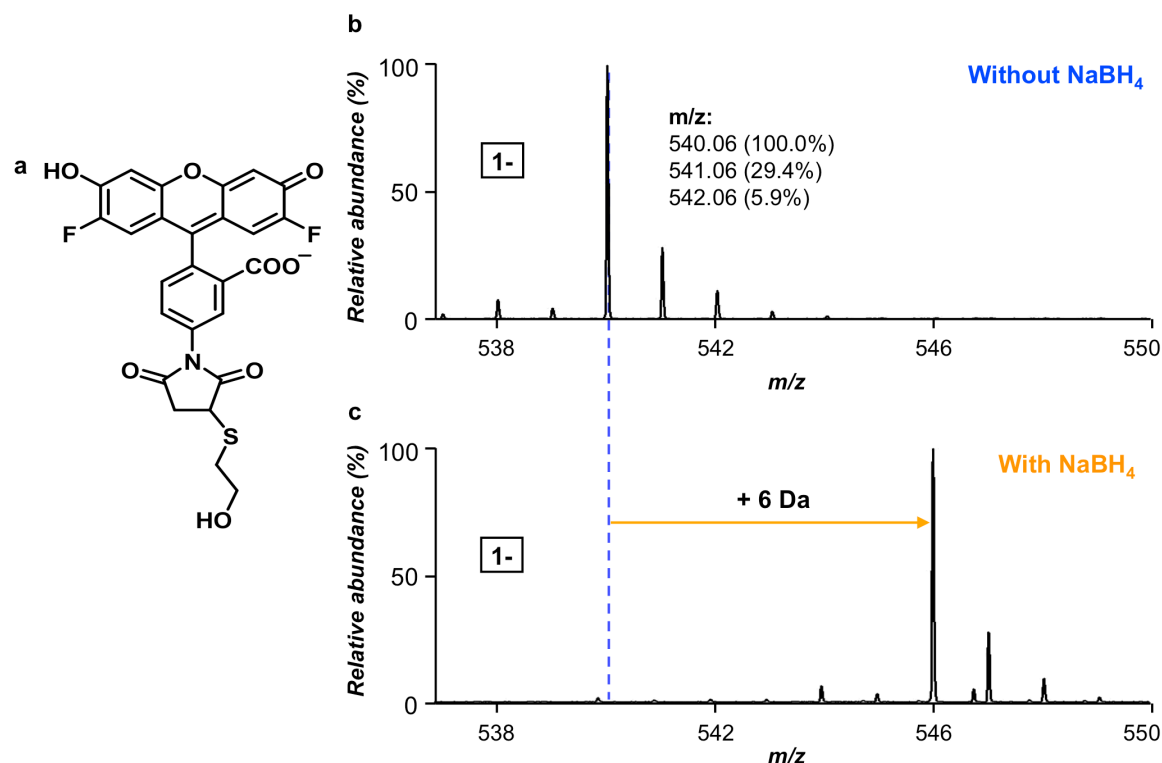


Figure S3. High resolution mass data for the small molecule donor chromophore before and after exposure to NaBH₄. (a) The structure of the dye after reaction with β -mercaptoethanol. A mass shift was observed throughout the charge ladder upon bleaching. Data for the -1 charge state are shown for the construct (b) before and (c) after bleaching, indicated an addition of six mass units.

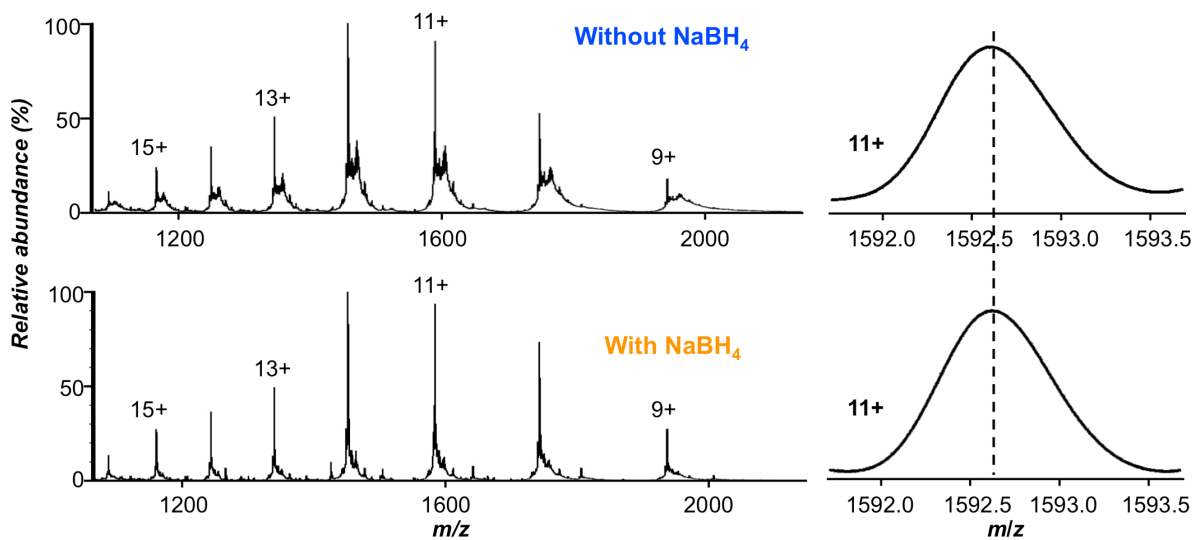


Figure S4. High resolution mass data for unmodified rTMVP before and after exposure to NaBH_4 . Data for the +11 charge state are shown for the protein before (top) and after (bottom) bleaching. No mass change was observed.

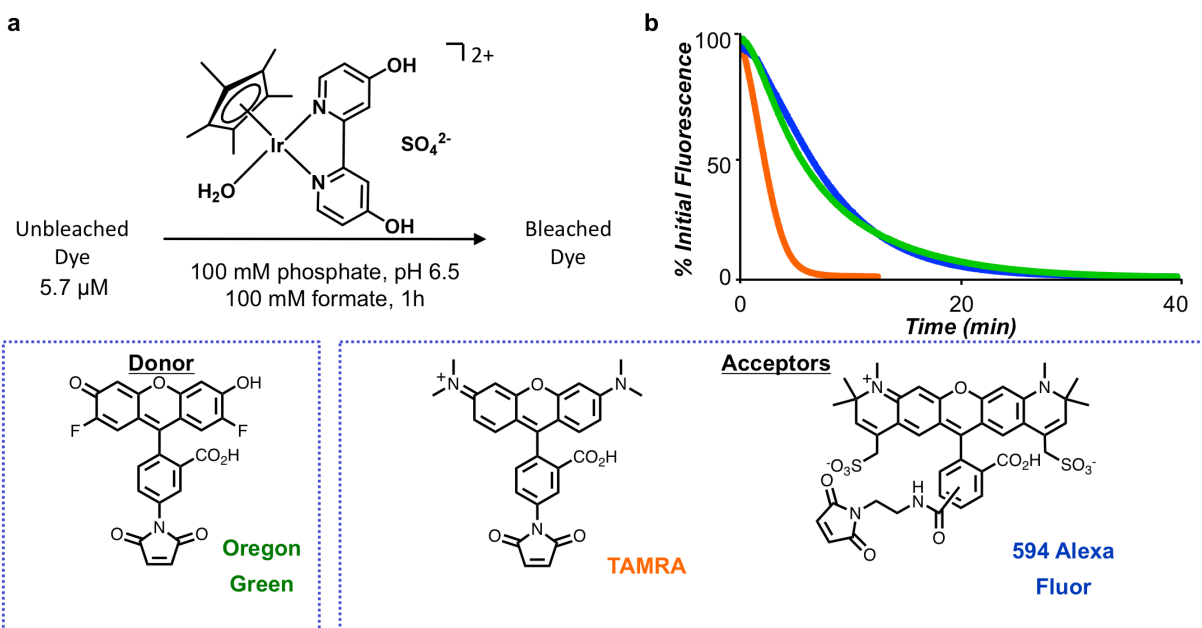


Figure S5. Substrate scope of Ir-mediated bleaching. (a) The iridium catalyst was added to a solution of free dye under buffer conditions identical to the protein reaction. (b) Bleaching occurred to completion in under half an hour for each of the three chromophores used in the construction of a TMV-based light harvesting system.

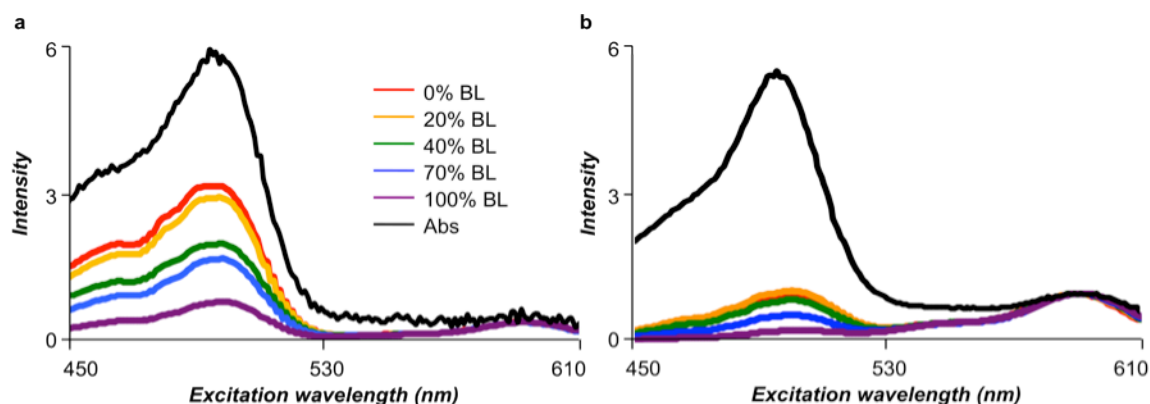


Figure S6. Excitation spectra monitoring the donor contribution to acceptor emission (615 nm) for a 16:1 system of **1** to **2** as a function of bleaching in (a) rod and (b) disk assembly states.

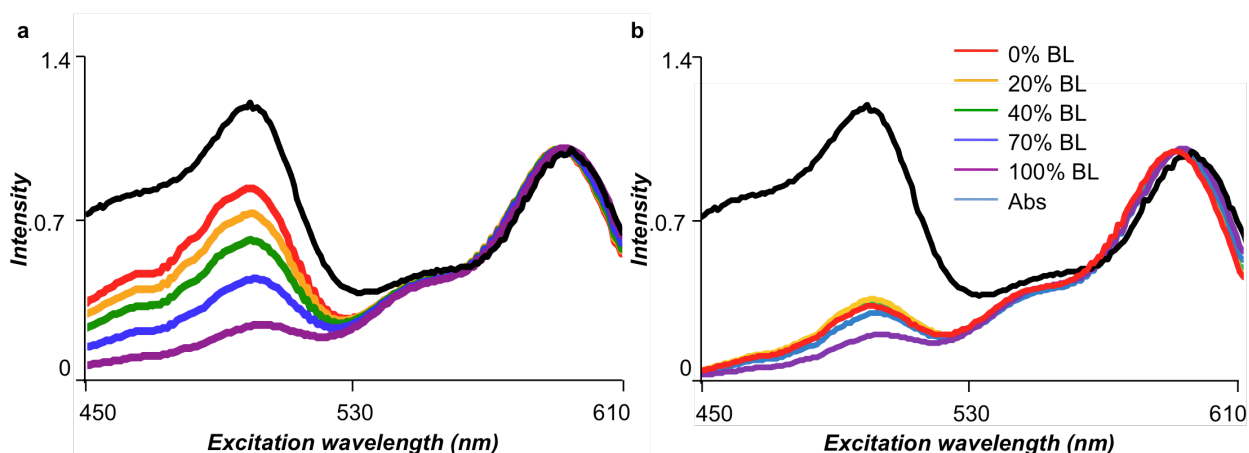


Figure S7. Excitation spectra monitoring the donor contribution to acceptor emission (615 nm) for a 2:1 system of **1** to **2** as a function of bleaching in (a) rod and (b) disk assembly states.

Calculation of Light Harvesting Efficiency for Systems Containing Bleached Donors. For each data point on the graphs in Figures 5c and d of the main text, the excitation spectrum was acquired by monitoring the acceptor emission at 615 nm. These full spectra appear in Figures S6 and S7. The "100% bleached" excitation spectrum (shown in purple) was subtracted to correct for residual acceptor absorbance and small remaining amounts of unbleached donors. The corrected excitation spectra were then compared to the absorbance spectrum of the "0% bleached" 16:1 or 2:1 system, as appropriate.

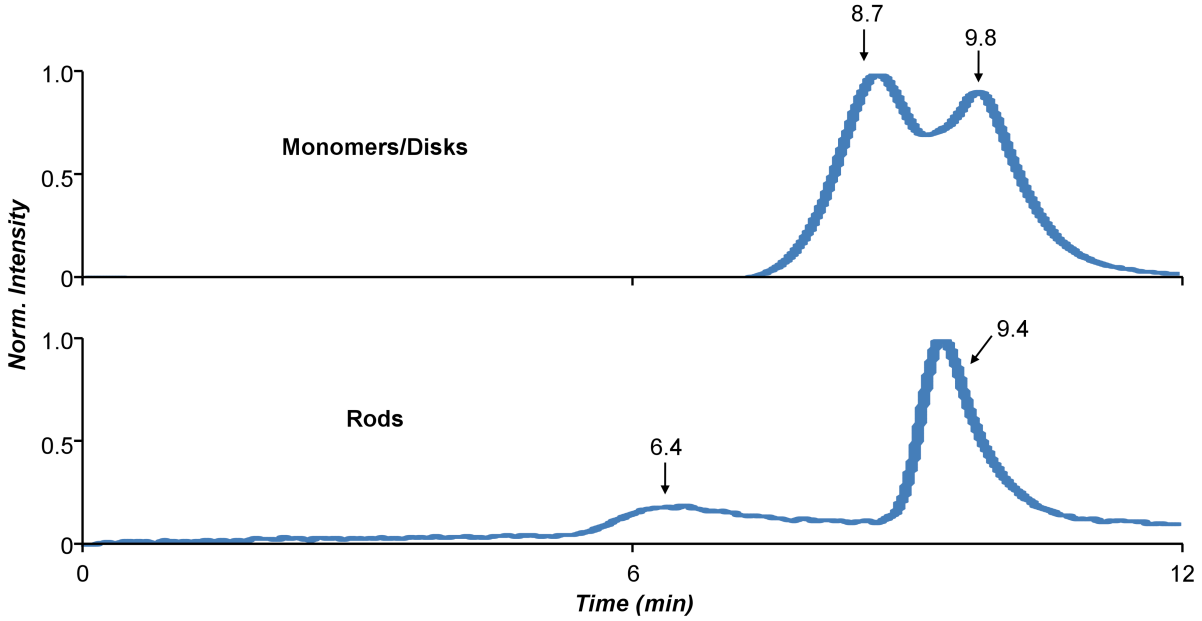


Figure S8. Size exclusion chromatography of the rod (a) and equilibrating disk and monomer (b) samples used to probe the photophysical properties of bleached donor only systems.

Calculation of the relative rates for vertical, horizontal, and diagonal transfer. According to Förster theory, the rate of transfer, k , is defined as:

$$k_T = \frac{J\kappa^2\lambda_D}{R^6\eta^4}$$

where \mathbf{J} is the overlap integral, η is the refractive index, λ_D is the emissive rate of the donor, and \mathbf{R} is the distance between the two chromophores. When determining the relative rate of transfer between two identical chromophores, as is the case of donor-to-donor transfer, this equation simplifies. For two Oregon Green chromophores held within TMV, \mathbf{J} , λ_D , and η^4 cancel, such that the relative rate depends only on κ^2 and \mathbf{R}^6 . For example, the rate of vertical transfer relative to horizontal transfer is given by:

$$\frac{k_V}{k_H} = \left(\frac{\kappa_V^2}{R_V^6} \right) \left(\frac{R_H^6}{\kappa_H^2} \right)$$

where \mathbf{k}_V is the rate of vertical transfer, \mathbf{k}_H is the rate of horizontal transfer, κ_V^2 is the orientation factor for a vertical donor-acceptor pair, \mathbf{R}_V is the end-to-end distance between two vertically stacked chromophores, κ_H^2 is the orientation factor for a horizontal donor-acceptor pair, and \mathbf{R}_H is the end-to-end distance between two chromophores horizontally adjacent to one another.

According to the accepted theory, the value for κ^2 can be determined for situations where the orientation of the donor and acceptor dipole moments is known according to the following relationship:

$$\kappa^2 = (\cos\theta_T - 3\cos\theta_D \cos\theta_A)$$

where θ_T is the angle between the donor and acceptor dipole moments, and θ_D and θ_A are the angles between the separation vector, R, and the donor and acceptor dipoles, respectively. In turn, θ_T is defined as

$$\theta_T = \sin\theta_D \sin\theta_A + \cos\theta_D \cos\theta_A$$

The angles necessary for this calculation were obtained from an image of the proposed chromophore arrangement and are summarized in the following table...”

Pathway	Θ_D	Θ_A	Θ_T
Horizontal	93.8	98.3	4.6
Vertical	7.6	9.1	16.6
Diagonal	18.1	22.9	4.8

Description of theoretical model. In order to model the energy transfer processes, we used a kinetic Monte Carlo algorithm where the probability of a given transfer was determined by the relative rate of that process. To model the geometry of the chromophores, we inspected the crystal structure of TMV and determined that the dyes were arranged in a square lattice (see, for example, Figure 7c). Each site is surrounded by eight nearest neighbors (one above, one below, one to the right, one to the left, two diagonally above, and two diagonally below). The monomers are arranged in a helix with a periodicity of 17, such that site i lies directly below site $i + 17$ and directly above site $i - 17$. A schematic depiction of the geometric arrangement of chromophores is shown in Figure S9a.

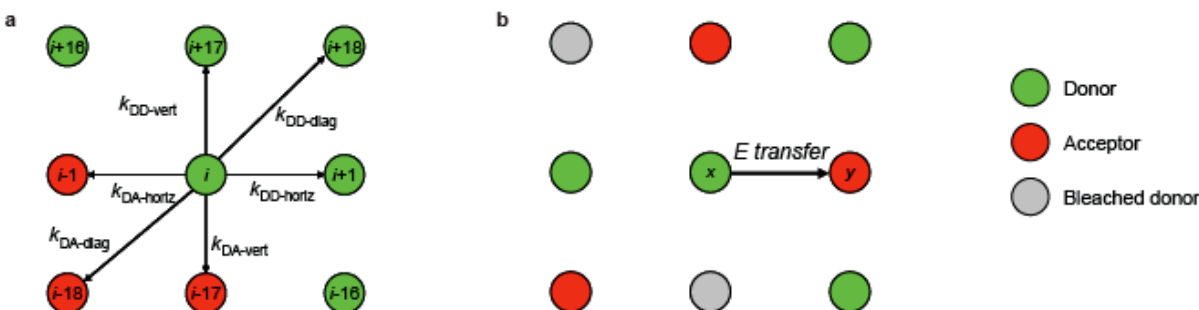


Figure S9. Schematic of the TMV system modeled. (a) At any given site i there are eight nearest neighbors, and the TMV helix has a periodicity of 17 such that site i lies below site $i + 17$ and above site $i - 17$. The energy transfer rates used in the model are indicated. (b) One possible arrangement of chromophores. For the probability of energy transfer between donor x and acceptor y , see the Supporting Information text.

The double-layer disks were modeled as an array of 34 units and the rods as an array of 5000 units. Each site was randomly assigned to be a donor (D) or acceptor (A) depending on the donor fraction ratio specified (0.94 for the 16:1 system and 0.67 for the 2:1 system). Each donor was then randomly assigned as bleached based on a specified bleach fraction ranging from 0 to 0.9. The simulation selected a random non-bleached donor to excite with a photon and tracked the fate of that excitation. Only one such excitation was simulated at a time, since we assumed that there was a low chance of a photon hitting an already excited chromophore given the low photon flux of the fluorimeter.

At any given site, the photon could, depending on the environment, be transferred to a non-bleached donor, transferred to an acceptor, or dissipated. The dissipation term lumped together two processes: thermal relaxation (non-fluorescent de-excitation) and fluorescence emission. For each arrangement of donors and acceptors 100,000 photons were simulated, and the simulation was run 100 times with a different, randomly assigned configuration of dyes each time in order to obtain the mean efficiencies and standard deviations reported. The efficiency of a given simulation was then defined as the number of photons that ultimately make it to an acceptor divided by the total number of photons simulation ($= 100,000$). Only photons that hit an active donor were considered (in order to more accurately determine the energy transfer pathways, even

at high fractions of bleached donors), but the efficiency was then scaled by the bleached fraction to correct for the fact that there were less active donors to absorb a photon to begin with, and to parallel the experimental calculation of efficiency (which compared the bleached system's excitation spectrum to the absorbance spectrum of the *unbleached* system).

The probability of a given energy transfer depended on the eight nearest-neighbors surrounding a site. Figure S9a defines the energy transfer rates possible: horizontal (“horiz”), vertical (“vert”), or diagonal (“diag”) transfer, between either two donors (DD) or a donor and acceptor (DA). Bleached sites were treated as inactive and thus unable to receive an excitation. At a given site, all possible energy transfer pathways were determined, and the simulation randomly selected a process depending on the relative rates available at that site. The probability P_j of a given transfer j depends on all the rate of that transfer relative to the sum of all possible rates at that site:

$$P_j = \frac{(k_j)}{\sum_i (k_i)} \quad (1)$$

For example, Figure S9b demonstrates one possible configuration of dyes, where the probability $P_{x \rightarrow y}$ of the energy transfer depicted between donor x and acceptor y is:

$$P_{x \rightarrow y} = \frac{k_{DA-horiz}}{k_{DA-horiz} + k_{DD-horiz} + k_{DA-vert} + 2k_{DD-diag} + k_{DA-diag} + k_{diss}} \quad (2)$$

The energy transfer rates were all normalized to that of the horizontal donor-donor transfer ($k_{DD-horiz}$), which was arbitrarily set to 1. The vertical and diagonal donor-donor transfer rates were determined from Fig. 7d. Previously, transient spectroscopy results indicated a transfer rate of 70 ps for donor-donor transfer and 187 ps for donor-acceptor transfer.⁴ Thus, to get the relative donor-acceptor rates in Fig. 7d, we scaled the donor-donor rates by a factor of 70/187.

Validation of model. In order to validate our model, we developed a mean-field approximation that allowed us to obtain an analytical result that could then be checked against the simulation. In this approximation, we first considered an array with no bleached donors and, for simplicity, all the directional energy transfer rates equal (i.e. $k_{DD-horiz} = k_{DD-vert} = k_{DD-diag} = k_{DD}$ and $k_{DA-horiz} = k_{DA-vert} = k_{DA-diag} = k_{DA}$, but $k_{DD} \neq k_{DA}$). The probability P_A that an excitation makes it to an acceptor in any given step is then:

$$P_A = \frac{n_A k_{DA}}{n_A k_{DA} + n_D k_{DD} + k_{diss}} \quad (3)$$

where n_A and n_D are the average numbers of acceptors and donors immediately surrounding the site of interest (and therefore $n_A + n_B = 8$ due to the square lattice geometry). Similarly, the probability that an excitation is transferred to a donor in a given step (P_D) is:

$$P_D = \frac{n_D k_{DD}}{n_A k_{DA} + n_D k_{DD} + k_{diss}} \quad (4)$$

For an excitation to make it to an acceptor after exactly n steps, there must be $n - 1$ donor-donor transfers followed by a donor-acceptor transfer in the n^{th} step. Thus, the probability P_n that an excitation makes it to an acceptor after exactly n steps is:

$$P_n = (P_D)^{n-1} (P_A) \quad (5)$$

The total probability that an excitation makes it to an acceptor (P_{acc}) is the summation of P_n over all values of steps n possible:

$$P_{acc} = \sum_{n=1}^{\infty} P_n = \sum_{n=1}^{\infty} (P_D)^{n-1} (P_A) = P_A \sum_{n=1}^{\infty} (P_D)^{n-1} \quad (6)$$

Shifting the summation index to $m = n - 1$ yields:

$$P_{acc} = P_A \sum_{m=0}^{\infty} (P_D)^m \quad (7)$$

However, the summation over m in Eq. 7 is an expression for a geometric series that converges to a finite solution:

$$\sum_{m=0}^{\infty} (P_D)^m = \frac{1}{1 - P_D} \quad (8)$$

Substituting Eq. 8 into Eq. 7 gives:

$$P_{acc} = \frac{P_A}{1 - P_D} \quad (9)$$

Plugging in for P_A and P_D from Eq. 3 and 4 yields:

$$P_{acc} = \frac{n_A k_{DA}}{n_A k_{DA} + n_D k_{DD} + k_{diss} - n_D k_{DD}} = \frac{n_A k_{DA}}{n_A k_{DA} + k_{diss}} \quad (10)$$

Dividing Eq. 8 by $n_A k_{DA}$, and remembering that n_A refers, in this mean-field approximation, to the *average* number of acceptors surrounding a given site (i.e. the acceptor fraction multiplied by eight, the total number of nearest neighbors) we get a final expression for the probability that an excitation reaches an acceptor:

$$P_{acc} = \frac{1}{1 + \frac{k_{diss}}{\langle n_A \rangle k_{DA}}} \quad (11)$$

If we let f be the donor fraction (and thus $(1-f)$ be the acceptor fraction), and let Z be the number of nearest neighbors ($=8$ in this geometry), Eq. 11 can be rewritten as:

$$P_{acc} = \frac{(1-f)\alpha_{iso}}{[1 + (1-f)\alpha_{iso}]} \quad (12)$$

where $\alpha_{iso} = Zk_{DA}/k_{diss}$.

Thus, we come to the conclusion that the probability depends only on two factors: 1) the average number of acceptors surrounding a given site and 2) the *ratio* of the dissipation rate and the donor-acceptor transfer rate. Interestingly, in this approximation the probability does *not* depend on the value of the donor-donor transfer rate because a donor-donor transfer leaves the simulation in the same state in which it started: that of an excited donor.

Figure S10 shows a series of plots at different values of $\langle n_A \rangle$ of P_{acc} (where P_{acc} is identical, by definition, to the efficiency used in earlier plots) vs. the ratio k_{diss}/k_{DA} . The values match very closely for all values of $\langle n_A \rangle$ and k_{diss}/k_{DA} examined, indicating that our model is performing as expected. In addition, changing the value of k_{DD} in the simulation had a negligible effect on the efficiency (approaching the limit of *no* effect predicted by our mean-field approximation), further validating the model.

For all the mean-field simulations in Figure S10, a rod with 5000 units was used in order to best approximate the “bulk” environment needed by the mean-field approximation, and 100,000 photons were simulated. Five simulations were run for each value of $\langle n_A \rangle$ and $k_{\text{diss}}/k_{\text{DA}}$ and the average efficiency of those runs was taken as P_{acc} . The extremely low variability of the efficiency in rods (see Figure 8c), however, meant that even five runs were sufficient to get accurate statistics.

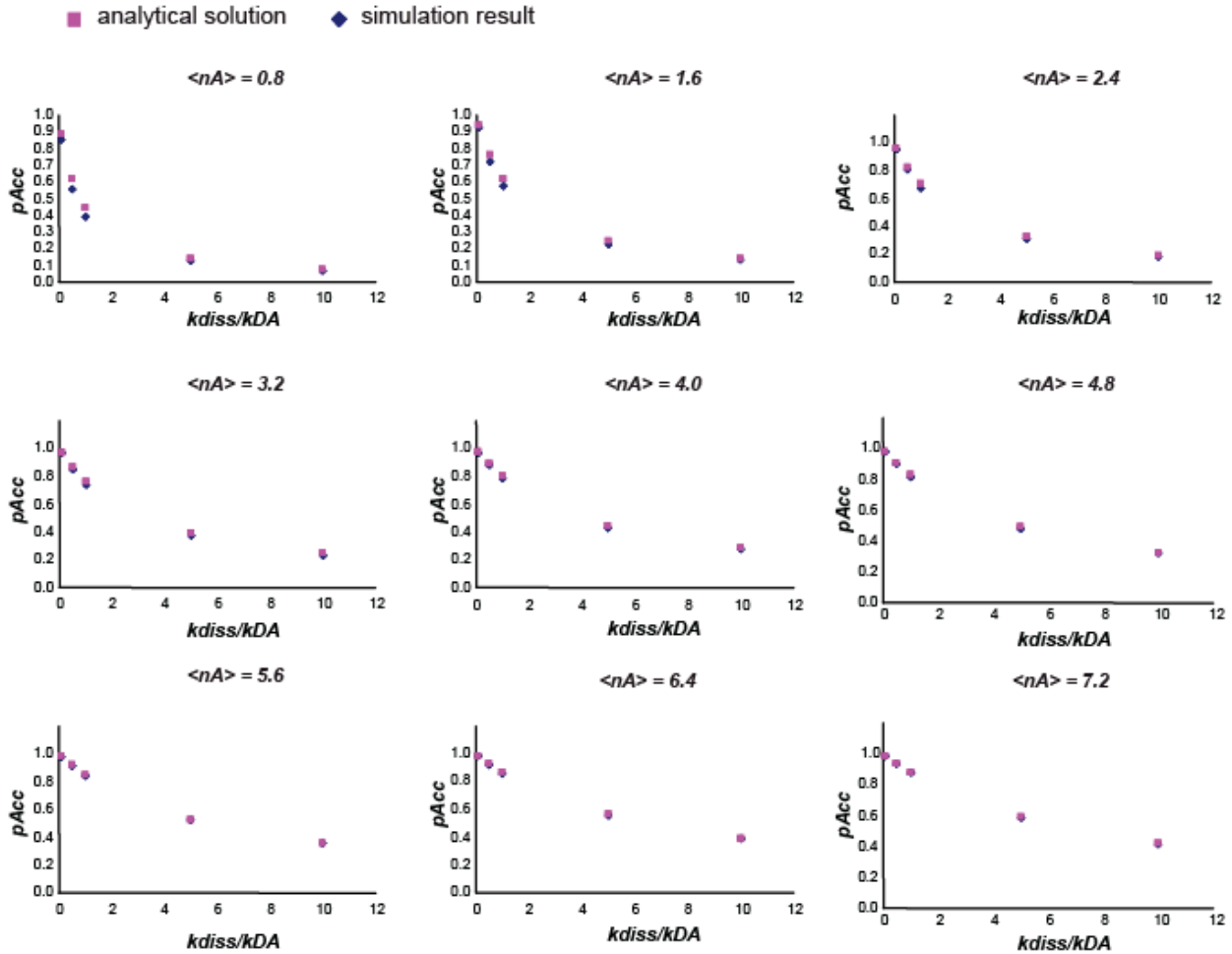


Figure S10. Mean-field solution results and comparison with experiment. The probability of an excitation reaching an acceptor from simulation closely matches the result obtained from the analytical solution for a wide range of values of $\langle n_A \rangle$ and $k_{\text{diss}}/k_{\text{DA}}$. The simulation was run at values of $k_{\text{diss}}/k_{\text{DA}} = 0.1, 0.5, 1, 5$, and 10 . As the value of $k_{\text{diss}}/k_{\text{DA}}$ increases, the difference between simulation and results decreased, so we did not need to validate the model beyond $k_{\text{diss}}/k_{\text{DA}} = 10$.

Extension to anisotropic energy transfer rates. In a similar manner, if we do *not* assume isotropic transfer rates, but rather the different horizontal, vertical, and diagonal transfer rates used in the actual simulation, we need to make the following substitutions:

$$n_A k_{DA} \Rightarrow \sum_{\gamma} n_{A-\gamma} k_{DA-\gamma} \quad (13)$$

$$n_D k_{DD} \Rightarrow \sum_{\gamma} n_{D-\gamma} k_{DD-\gamma} \quad (14)$$

where $\gamma = \text{horiz, vert, diag}$. Making these appropriate substitutions in Eq. 3 and 4, and following the same derivation outlined above for the isotropic case, we come to the anisotropic analogue of Eq. 11:

$$P_{acc} = \frac{1}{1 + \frac{k_{diss}}{\sum_{\gamma} n_{A-\gamma} k_{DA-\gamma}}} \quad (15)$$

Also, we have the following relation:

$$\sum_{\gamma} n_{A-\gamma} k_{DA-\gamma} = (1-f) \sum_{\gamma} Z_{\gamma} k_{DA-\gamma} \quad (16)$$

where, once again, f is the donor fraction (so $1-f$ is the acceptor fraction) and Z is the number of neighboring sites in a given direction (horizontal, vertical, or diagonal). Inserting Eq. 16 into Eq. 15 and rearranging, we arrive at the following analogue of Eq. 12, reported as Eq. 2 in the main text:

$$P_{acc} = \frac{(1-f)\alpha_{aniso}}{[1 + (1-f)\alpha_{aniso}]} \quad (17)$$

where (as shown in Eq. 3 of the main text):

$$\alpha_{aniso} = \frac{\sum_{\gamma} Z_{\gamma} k_{DA-\gamma}}{k_{diss}} = \frac{(Z_{horiz} k_{DA-horiz} + Z_{vert} k_{DA-vert} + Z_{diag} k_{DA-dia})}{k_{diss}}$$

In the TMV geometry, $Z_{horiz} = 2$ (for both disks and rods), $Z_{vert} = 2$ for rods and 1 for disks, and $Z_{diag} = 4$ for rods and 2 for disks. The results of this anisotropic model are indicated by the lines in Figure 8a,b.

Derivation of analytical result for 1-D array. If energy transfer rates are nonzero only between immediate neighbors in an array of fluorophores, a domain of donors entirely bounded by defects forms a corral inside which excitations are topologically trapped and must eventually dissipate. The prevalence of such corrals depends strongly on dimensionality, i.e. on the degree of connectivity between non-adjacent fluorophores via intervening donors. The very limited

connectivity of a linear array generates a significant number of corrals even at relatively low defect density, as we quantify below.

Excitation at a randomly selected donor D^* in an infinite linear array is trapped in this fashion if, proceeding outward from D^* , a defect is encountered before an acceptor, both to the left and to the right. Because fluorophore compositions in the two directions are statistically independent, the probability P_{corral} that D^* resides in a corral is a product of one-sided probabilities:

$$P_{\text{corral}} = p_{\text{left}} p_{\text{right}} = p_{\text{right}}^2 \quad (18)$$

where p_{right} is the probability that the sequence of fluorophores to the right of D^* includes a defect before the first acceptor; p_{left} is similarly defined and is identical to p_{right} by symmetry.

We can evaluate p_{right} simply by enumerating the relevant compositional possibilities: (1) the right-hand neighbor of D^* is defective, which occurs with probability fx ; (2) the right-hand neighbor of D^* is an active donor and the subsequent site is defective, with probability $f(1-x)fx$; ...; (n) n consecutive neighbors to the right of D^* are active, followed by a defect, with probability $[f(1-x)]^n fx$; etc. Summing these probabilities, we have

$$p_{\text{right}} = f \{ 1 + f(1-x) + [f(1-x)]^2 + \dots \} = \frac{fx}{1 - f(1-x)} \quad (19)$$

Eq. 1 in the main text follows from substituting Eq. 19 into Eq. 18.

Supporting Information References

1. Shire S. J., McKay P., Leung D.W., Chachianes G.J., Jackson E., Wood W.I. *Biochem.* **1990**, 29, 5119-5126.
2. Bradford, M. *Anal. Biochem.* **1976**, 72, 248-254.
3. Dadci, L.; Elias, H.; Frey, U.; Hörnig, A.; Koelle, U.; Merbach, A. E.; Paulus, H.; Schneider, J. S. *Inorg. Chem.* **1995**, 34, 306.
4. Dale R. E., Eisinger J., Blumberg W. E. *Biophys. J.* **1979**, 26, 161-193.
5. Miller R.A., Presley A.D., Francis M.B. *J. Am. Chem. Soc.* **2007**, 129, 3104-3109.